Available online at www.sciencedirect.com

ScienceDirect

Geochimica et Cosmochimica Acta 332 (2022) 355–368

Geochimica et Cosmochimica Acta

www.elsevier.com/locate/gca

Iron isotope fractionation in anoxygenic phototrophic Fe(II) oxidation by *Rhodobacter ferrooxidans* SW2

Xiaohua Han [a,c,d,*], Yongsheng He [b,*], Jinhua Li [a,d], Andreas Kappler [c], Yongxin Pan [a,d]

[a] *Biogeomagnetism Group, Key Laboratory of Earth and Planetary Physics, Institute of Geology and Geophysics, Chinese Academy of Sciences, Beijing 100029, China*

[b] *State Key Laboratory of Geological Processes and Mineral Resources, China University of Geosciences, Beijing 100083, China*

[c] *Geomicrobiology, Center for Applied Geosciences, University of Tuebingen, Schnarrenbergstrasse 94-96, 72076 Tuebingen, Germany*

[d] *College of Earth and Planetary Sciences, University of Chinese Academy of Sciences, Beijing 100049, China*

Received 22 January 2022; accepted in revised form 23 June 2022; Available online 30 June 2022

Abstract

Microbially mediated Fe(II) oxidation is one of the most important pathways of Fe redox cycling on both present and early Earth. It was proposed to participate in iron formations (IFs) deposition under oxygen-depleted oceanic conditions before the Great Oxidation Event (GOE). Fe isotopic records in IFs provide important archives for the redox state of iron pool in paleo oceans. There have been a number of iron-oxidizing experiments which used bacteria with different metabolic pathways. However, it still needs further research on how and to what extent Fe isotopes are fractionated during Fe(II) oxidation mediated by the anoxygenic phototrophic Fe(II)-oxidizer, as well as its implications for the redox state of iron pool in paleo oceans. Here, we report Fe isotope fractionation between $Fe(II)_{aq}$ and Fe(III) (oxyhydr)oxides precipitates produced by the anoxygenic phototrophic Fe(II)-oxidizer *Rhodobacter ferrooxidans* SW2 at ambient temperature (20 °C). Mössbauer spectroscopy analyses indicated that the final mineral product was ferrihydrite. The corrected Fe isotope fractionation between $Fe(II)_{aq}$ and precipitates ($\Delta^{56}Fe_{precipitate-Fe(II)aq}$) ranged from ca. -0.37 ± 0.04‰ (2se, N = 2) after 1 day of cultivation to 2.96 ± 0.17‰ (2se, N = 2) after 22 days of cultivation. The observed fractionation cannot be explained by neither a simple Rayleigh nor equilibrium process, but likely recorded a process from an isotopic disequilibrium reaching complete or near-complete equilibrium during 22 days of cultivation. The lower precipitation rate after 7 days, small size of oxidation products and dissolution-oxidation-reprecipitation processes probably promoted isotope exchange overwhelming the kinetic effect, resulting in a final isotope equilibrium between precipitates and $Fe(II)_{aq}$. It revealed that the ferrihydrite produced by Fe(II) oxidation by anoxygenic photoferrotrophy could reach Fe isotope equilibrium relatively easily, thus IFs may record Fe isotope equilibrium with the fluids from which they precipitated, i.e. in some cases solely from seawater in Archean oceans.

Keywords: Iron biogeochemical cycling; Anoxygenic photosynthetic Fe(II) oxidation; Iron isotope fractionation; Redox state of paleo oceans

1. INTRODUCTION

Geochemical cycling of iron (Fe) is important in modern and ancient Earth and principally controlled by the prevalent changing redox conditions (e.g., Beard et al., 1999; Rouxel et al., 2005; Johnson et al., 2008a). Large Fe isotope fractionation occurs during oxidation of dissolved ferrous

* Corresponding authors at: Biogeomagnetism Group, Key Laboratory of Earth and Planetary Physics, Institute of Geology and Geophysics, Chinese Academy of Sciences, Beijing 100029, China (X. Han); State Key Laboratory of Geological Processes and Mineral Resources, China University of Geosciences, Beijing 100083, China (Y. He).

E-mail addresses: hanxiaohua@mail.iggcas.ac.cn (X. Han), heys@cugb.edu.cn (Y. He).

https://doi.org/10.1016/j.gca.2022.06.034
0016-7037/

Fe ($Fe(II)_{aq}$) and precipitation of Fe(III) (oxyhydr)oxides (e.g., Johnson et al., 2008b). Therefore, Fe isotopic records in Precambrian iron formations (IFs) can provide important archives for the oxidation extent of the iron pool in the fluids from which the minerals precipitated and accordingly the redox state of paleo-oceans (e.g., Rouxel et al., 2005; Li et al., 2013; Raye et al., 2015; Raiswell et al., 2018). For example, the highly positive $\delta^{56}Fe$ values up to +2.63‰ of the Duffer Formation from the Pilbara Craton indicated a very low degree of Fe(II) oxidation and thus a low O_2 level in the ocean and atmosphere during the time of precipitation at ca. 3.46 Ga (Li et al., 2013). While the near-zero $\delta^{56}Fe$ values for magnetite from the Hamersley-Transvaal IFs were interpreted to be inherited from ferric (oxyhydr)oxide minerals that were likely precipitated during near complete oxidation of the upper seawater column at ca. 2.5 Ga (Johnson et al., 2008a).

Microbially mediated Fe(II) oxidation is one of the most important pathways of Fe redox cycling in the era before the Great Oxidation Event (GOE). The deposition mechanisms for IFs were classically interpreted to reflect Fe(II) oxidation related to indirect and/or direct microbial activities, i.e. molecular oxygen produced by cyanobacteria and/or anoxygenic photoautotrophic bacteria under anoxic conditions (Cloud, 1973; Garrels et al., 1973; Konhauser et al., 2002; Kappler et al., 2005). In particular, anoxygenic Fe (II)-oxidizing phototrophs are among the most ancient photosynthetic organisms (Xiong, 2007), and can harvest energy from light and electrons from oxidation of Fe(II) (Ehrenreich and Widdel, 1994), producing ferric (oxyhydr)oxides that could have been preserved in IFs (Kappler et al., 2005; Konhauser et al., 2017). Recently, as an alternative to the oxidization model, the deposition and early growth of reduced Fe(II)-dominated phases (greenalite, siderite) that were progressively replaced by iron oxides during burial and subsequent uplift and oxidation by surface-derived fluids was proposed (Rasmussen et al., 2014; Johnson et al., 2018; Rasmussen and Muhling, 2018). Although a dominant role of anoxygenic Fe(II)-oxidizing phototrophs in oxidizing Fe(II) in the photic zones in pre-GOE anoxic environments is widely accepted, the question how and to what extent Fe isotopes fractionated during Fe(II) oxidation mediated by these microorganisms still need further research.

A better understanding of Fe isotope fractionation during precipitation of Fe(III) (oxyhydr)oxides via $Fe(II)_{aq}$ oxidation is a prerequisite to trace the redox state of ancient seawater and atmosphere using Fe isotopes. Isotope equilibrium between aqueous ferrous and ferric species (i.e., $Fe(II)_{aq}$ and $Fe(III)_{aq}$) can be reached in minutes, and the equilibrium fractionation factor (i.e., $\Delta^{56}Fe_{Fe(III)aq\text{-}Fe(II)aq}$) at room temperature has been calibrated to be ca. 2.9‰ with $[Fe^{II}(H_2O)_6]^{2+}$, $[Fe^{III}(H_2O)_6]^{3+}$ and $[Fe^{III}(H_2O)_{6-n}(OH)_n]^{3-n}$ as the dominant species (Johnson et al., 2002; Welch et al., 2003). Fractionation processes and factors between Fe(III) (oxyhydr)oxides and $Fe(II)_{aq}$ have also been intensively investigated by biotic and abiotic experiments, which showed more complexities (e.g., Beard et al., 2010; Kappler et al., 2010; Wu et al., 2010; Frierdich et al., 2014; Frierdich et al., 2019). For example, equilibrium fractionation factors between Fe(III) (oxyhydr) oxides and $Fe(II)_{aq}$ varied with the initial mineral particle size (Beard et al., 2010; Frierdich et al., 2014, 2019). Except a large particle size, the dissolved silica (which was high or even saturated in Archean seawater) could also hinder complete isotope exchange between Fe(III) (oxyhydr) oxides and aqueous Fe(II), reflecting blockage of surface Fe sites by sorbed silica (Wu et al., 2011, 2012). Additionally, kinetic effects upon rapid precipitation played a significant role in Fe isotope fractionation during biotic and abiotic Fe (II) oxidation and precipitation experiments, which could result in Fe-bearing minerals with isotope compositions apparently lighter than those expected for equilibrium (e.g., Skulan et al., 2002; Croal et al., 2004). Therefore, it is crucial to constrain equilibrium fractionation factors between Fe(III) (oxyhydr)oxides and the dissolved Fe(II) and to what extent Fe isotope equilibrium may be approached during precipitation of Fe(III) (oxyhydr)oxides from the fluids (e.g., seawater) for deciphering the redox state of paleo oceans and atmosphere from IFs.

To better understand Fe isotope fractionation between Fe minerals and seawater before GOE, we have used the anoxygenic phototrophic Fe(II)-oxidizer *Rhodobacter ferrooxidans* SW2 as a model microorganism to study the Fe isotope fractionation which may occur in paleo-oceans. The final minerals produced by SW2 were analyzed by electron microscopy, Mössbauer spectroscopy and magnetic measurements. The $\delta^{56}Fe$ values have been determined for coexisting $Fe(II)_{aq}$, intermediate Fe species (i.e. adsorbed, incorporated Fe into precipitates), and precipitates produced from Fe(II) oxidation by SW2, with the purpose of assessing Fe isotope fractionation processes involved in this type of microbially-mediated Fe(II) oxidation. This study recorded Fe isotope fractionation values between $Fe(II)_{aq}$ and Fe(III) (oxyhydr)oxides shifting from disequilibrium to complete or near-complete equilibrium during a 22-days incubation. Combined with previous literatures on the precipitation rates of Fe(III) minerals in Archean and Paleoproterozoic oceans, we further discussed our data in the context of Fe isotopic data of IFs.

2. MATERIALS AND METHODS

2.1. Bacterial strain and culture medium

Rhodobacter ferrooxidans SW2 was isolated from ponds in Schaumburger Wald, Hanover region, Germany (Ehrenreich and Widdel, 1994) and cultivated in anoxic medium. The medium was buffered at pH 7.0 with bicarbonate. One milliliter each of a vitamin solution, trace element solution and selenite-tungstate stock solution were added to 1 L medium (Ehrenreich and Widdel, 1994). Before cultivation, an anoxic $FeCl_2$ stock solution was added to the medium targeting a final Fe(II) concentration of ~10 mM. Greyish-green precipitates formed during addition of $FeCl_2$, inferred to consist of $Fe(OH)_2$, $FeCO_3$ and $Fe_3(PO_4)_2$ based on the anions present in the medium including OH^-, CO_3^{2-} and PO_4^{3-} (Hohmann et al., 2010). The medium was stood still in 4 °C for 24 h to allowed the supersaturated precipitation of Fe(II) minerals. After

which, the medium was filtered with a 0.22-μm filter in an anoxic chamber, leaving a clear solution with ca. 3 mM remaining $Fe(II)_{aq}$. Compared with Hohmann et al. (2010), in which the same medium and filtration process were used, 40 μM phosphate and similar 3–4 mM dissolved Fe(II) was left in the solution. 50 mL medium was transferred into the 100-mL serum bottle and the headspace was flushed with N_2:CO_2 (v:v, 80:20). SW2 cells were firstly inoculated with H_2 to avoid bringing any Fe minerals in medium from the inoculum, then transferred into the Fe (II)-containing medium and cultured at 20 °C under light intensity of 400 lux (8 mmol quanta m^{-2} s^{-1}) for 22 days. Experiments were conducted with three independent biological replicates (referred as SW2-1, SW2-2 and SW2-3).

2.2. Sampling and Fe concentration analyses

During incubation, 1 mL of culture slurry was taken from the three serum bottles using sterile syringes at intervals of 0, 1, 4, 7, 14, and 22 days in an anoxic glovebox (COY-7000220A, USA). The sample slurry was centrifuged at 13,400 rpm for 5 mins. The supernatant was collected as an aqueous fraction. Previous studies suggested that adsorbed and incorporated Fe species into precipitates existed as an intermediate pool in precipitates (Icopini et al., 2004; Jang et al., 2008; Swanner et al., 2015; Wu et al., 2017). To remove these adsorbed and incorporated Fe species from precipitates, the precipitates were washed by anoxic H_2O (bubbled with N_2) and 0.5 M anoxic sodium acetate (NaAc, pH adjusted to 4.85 with acetic acid) sequentially. The precipitates obtained at 1d were only washed with anoxic H_2O but without NaAc, given the small amount of precipitates left after the anoxic H_2O washing step. One mL of 1 M HCl was added to the supernatant (Fe_{aq}) and to the leachates (Fe_{H2O} and Fe_{NaAc}) to stabilize Fe^{2+} in the solution (Porsch and Kappler, 2011). The washed precipitates (Fe_{ppt}) were dissolved in 6 M HCl, and then added to 1 mL 1 M HCl for stabilization. The sampling and separation procedures for samples taken during oxidation of Fe(II) by *Rhodobacter ferrooxidans* SW2 were summarized in Fig. S1. Both Fe(II) and total Fe concentrations were analyzed for the different fractions (Fe_{aq}, Fe_{H2O}, Fe_{NaAc} and Fe_{ppt}) by the ferrozine assay (Stookey, 1970). External precision was better than ±1% (2SD, N = 25) based on repeated analysis of the standard solutions. The Fe(III) concentrations were calculated by subtraction of Fe(II) from the total Fe.

2.3. Electron microscopy analyses

Scanning electron microscopy (SEM) and transmission electron microscopy (TEM) analyses were used to investigate the microorganism-mineral associations in SW2 cultures and the crystal morphology of the final mineral products after 22 days of cultivation. Both SEM and TEM analyses were performed in the Electron Microscopy Laboratory at Institute of Geology and Geophysics, Chinese Academy of Sciences (IGGCAS), Beijing. A drop of culture slurry was collected and washed with high purity H_2O to remove other salts stemming from the growth medium. The washed samples were placed on an ultrathin carbon-coated copper grid. The SEM observations were done in a LEO 1450 VP (Germany) with a voltage of 1.5 kV. The TEM imaging and selected area electron diffraction (SAED) pattern analyses were performed on a JEM-2100HR TEM (JEOL, Japan) at an acceleration voltage of 200 kV.

2.4. Mössbauer spectroscopy

For Mössbauer spectroscopic analysis, 2 mL of culture slurry was taken from the serum bottle after 22 days of cultivation, and filtered on a 0.45 μm filter membrane and embedded in the Kapton tape in the anoxic glovebox (100 % N_2). Mössbauer spectroscopy analyses were carried out in the Key Laboratory of Petroleum Resource in Lanzhou, Gansu Province. Samples were kept in a sealed anoxic glass bottle before measurement. The Mössbauer spectra was measured at 295 K using a MA-260 (Bench MB-500) Mössbauer spectrometer with a γ-ray source of 0.925 GBq, ^{57}Co/Rh. The measurement and curve fitting procedures were described elsewhere (Matsuo et al., 1994). The spectra were fitted to Lorentzian line shapes with standard line shape fitting routines using WinNoroms-for-Igor software.

2.5. Iron isotope analysis

Iron isotope analysis was conducted in Isotope Geochemistry Laboratory at China University of Geosciences, Beijing, following the procedures previously established (Dauphas et al., 2009; He et al., 2015; Zhu et al., 2018). Samples were sequentially fluxed by H_2O_2 and aqua regia to remove the organic matter and oxidize all Fe to Fe (III), and then dissolved in 6 mol l^{-1} HCl. Iron was purified using 1 mL AG1X-8 resin (200–400 mesh chloride form, Bio-Rad, Hercules, CA, USA) in HCl media. Matrix elements were removed by 8 mL of 6 mol l^{-1} HCl, and Fe was then collected by 10 mL of 0.4 mol l^{-1} HCl. The same column procedure was repeated twice to ensure complete elimination of the matrices. The final Fe eluate was dried and treated by 100 μl of concentrated HNO_3, and then finally dissolved in 3% HNO_3 for isotopic analysis. Recovery of Fe was >99.5%, and the Fe blank in whole procedure was 10 ng during the course of this study, which is <0.01% of the processed samples and thus considered negligible. Iron isotopic measurements were conducted on a Thermo-Finnigan Neptune Plus MC-ICP-MS. ^{53}Cr, ^{54}(Fe + Cr), ^{56}Fe, ^{57}Fe, ^{58}(Fe + Ni) and ^{60}Ni isotopes were collected in the static mode by Faraday cups at Low 3, Low 1, Central, High 1, High 2 and High 4 positions, respectively. The instrument mass bias was corrected by Ni-doping and standard-sample-bracketing (Zhu et al., 2018). Data are reported in δ notions relative to IRMM-014:

$$\delta^{x}\mathrm{Fe} = \left(\frac{{}^{x}Fe/{}^{54}Fe_{sample}}{{}^{x}Fe/{}^{54}Fe_{IRMM-014}} - 1\right) \times 1000 \quad (1)$$

where x can be 56 or 57. Each sample solution was measured 3–5 times on MC-ICP-MS, and the mean values

and relevant two standard errors of the mean were given in Table S2. The internal errors were calculated after Dauphas et al. (2009) and He et al. (2015), considering uncertainties rising from both the mass spectrometry measurement and the chemical procedures. The reproducibility (2SD) and accuracy of δ^{56}Fe were estimated to be ≤0.05‰ based on long-term measurement on geological reference standards (He et al., 2015; Zhu et al., 2018). USGS standard BCR-2 and BHVO-2 measured during the course of this study yielded δ^{56}Fe of 0.081 ± 0.027‰ and 0.112 ± 0.027‰ respectively, which agreed with those values reported in Craddock and Dauphas (2011) (BCR-2, 0.091 ± 0.011‰; BHVO-2, 0.114 ± 0.011‰) and Chen et al (2017) (BCR-2, 0.090 ± 0.021‰; BHVO-2, 0.102 ± 0.026‰) within quoted errors.

3. RESULTS

3.1. Microscopic analysis of cell–mineral aggregates

SEM and TEM observations showed that strain SW2 cells were rod-shaped, 1.5–2.3 μm in length and ~0.5 μm in width (Fig. 1a, b). The Fe(III) precipitates appeared as aggregates of hundreds of nanometer in size and consisted of particles in irregular shapes. These particles could be poorly crystalline minerals, likely ferrihydrite, indicated by two coarse rings in the selected area electron diffraction (SAED) pattern (Fig. 1c). The Fe(III) precipitates associated with the cell wall randomly, but they did not cover it entirely (Fig. 1b), although that the cell surfaces were usually negatively charged and the Fe(III) particles were positively charged (Hegler et al., 2010; Hohmann et al., 2010). This suggests that Fe(III) precipitated away from the cells during Fe(II) oxidization which possibly resulted from bacteria cells creating a pH microenvironment to keep the Fe (III) in solution in close cell vicinity (Hegler et al., 2010), a gradient of the Fe oxidation state at the submicrometer scale (Miot et al., 2009b) and/or excreted exopolymeric substances (EPS) that bind Fe(III) (Wu et al., 2014).

3.2. Fe mineralogy

Mössbauer spectra obtained at 295 K for the precipitates after 22 days of cultivation showed a paramagnetic doublet (Table 1, Fig. 2). The average parameters were obtained by fitting the spectra with one doublet. The center shift and quadrupole splitting of this doublet were 0.37 mm s^{-1} and 0.71 mm s^{-1}, which consistent with that of biogenic ferrihydrite produced by the marine Fe(II)-oxidizing phototroph *Rhodovulum iodosum* and by the freshwater Fe(II)-oxidizing phototroph *R. ferrooxidans* SW2 reported in previous studies (Eickhoff et al., 2014; Swanner et al., 2015). The mineralogical result was also consistent with the following Fe concentration result which showed the high Fe(III)/$\sum$$Fe_{ppt}$ (98–99.5%) of final mineral products, suggesting that Fe(III) minerals were dominant in the precipitates. Schwertmann and Cornell (2000) has shown that poorly crystalline ferrihydrite in dry form was stable for years. The identification of ferrihydrite in final mineral products by Mössbauer spectroscopy analysis suggested that there was no secondary mineral transformation during the transportation to the laboratory in Lanzhou. Despite not being monitored, pH of the medium was buffered by bicarbonate and most likely changed insignificantly during the experiments (as shown by Hegler et al., 2008). Therefore, here we will not consider the role of pH changes on the stability of mineral phases.

3.3. Fe species, concentration and isotope compositions

Species and concentrations of all Fe fractions collected during Fe(II) oxidation varied over time (Table S1, Fig. 3). Total Fe concentrations of Fe_{aq} kept decreasing along with Fe(II) oxidation by SW2, while the total Fe concentration of Fe_{ppt} kept increasing as the accumulation of oxidation products. Except from the 14 d and 22 d samples, there was nearly no dissolved Fe(III) (i.e. $Fe(III)_{aq}$, and Fe (III)/$\sum$$Fe_{aq}$ < 8%) in the aqueous Fe fraction (Fe_{aq}) (Fig. 3a, e). Fe(III)/$\sum$$Fe_{aq}$ for 14d and 22d samples differed among the three independent biological replicates, ranging from 0.3% to 48% and from 12% to 24%, respectively. The high Fe(III)/$\sum$$Fe_{aq}$ in 14d and 22d samples indicated an abiotic oxidation of Fe_{aq} during sequential extraction of different Fe species. The abiotic oxidation of Fe_{aq} most likely occurred after harvest from the serum bottles, e.g., during moving aqueous Fe species by plastic pipette tips into different plastic tubes due to residual oxygen in these tips and tubes. In addition, ferrous Fe in low concentration in the aqueous solutions may be also less resistant to oxidation (see a detailed discussion in Appendix). For the

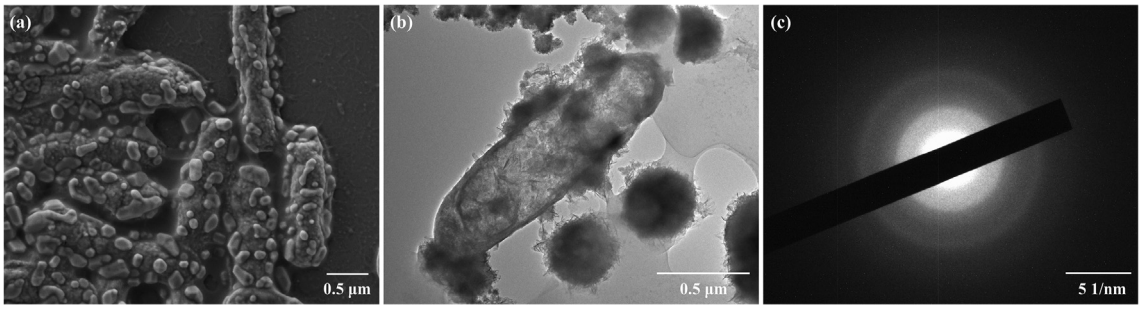

Fig. 1. Scanning (a) and transmission (b) electron micrographs of *R. ferrooxidans* SW2 and its final mineral products. A selected area electron diffraction (SAED) pattern for the final mineral products (c).

Table 1
Mössbauer spectroscopy parameters derived from fitting spectra obtained at 295 K for final oxidation products by *R. ferrooxidans* SW2, compared to biogenic ferrihydrite which were determined previously. CS – center shift; ΔE_Q – quadrupole splitting; χ^2 – error of the fit; NA – not available.

Sample	CS (mm/s)	ΔE_Q (mm/s)	χ^2	Reference
Oxidation products by *R. iodosum*	0.38	0.74	NA.	Swanner et al., 2015
Oxidation products by SW2	0.37	0.76	NA.	Eickhoff et al., 2014
Oxidation products by SW2	0.37	0.71	1.72	*this study*

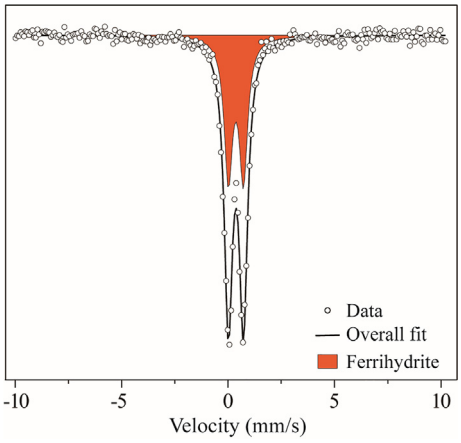

Fig. 2. ^{57}Fe Mössbauer spectra collected at 295 K for the final minerals produced by *R. ferrooxidans* SW2. The raw data, fit of the data and the sub-spectra of the fit are shown as data points, solid line and filled orange area, respectively. (For interpretation of the references to colour in this figure legend, the reader is referred to the web version of this article.)

precipitates (Fe_{ppt}), except the 1d and 4d samples, Fe(III)/$\sum Fe_{ppt}$ was >95% after a two-step washing procedure (Fig. 3d, h). Fe(III)/$\sum Fe_{ppt}$ for 1d samples ranged from 13% to 40%, and for 4d samples from 74% to 82%. In the Fe_{H2O} and Fe_{NaAc} fractions, the Fe was present as a mixture of Fe(II) and Fe(III) (Fig. 3b, c and f, g). Although more precipitates were produced, the total Fe concentration of Fe_{H2O} and Fe_{NaAc} fractions decreased over time. The Fe(II) concentration of the abiotic control experiment was basically unchanged (Fig. S3), suggesting there was no chemical oxidation (such as UV-induced photochemical $Fe(II)_{aq}$ oxidation) in all batch reactors.

Iron isotope compositions were measured for two of the biological replicates (SW2-2 and SW2-3) (Table 2; Fig. 4). Detailed data are included in the Table S2. Overall, the two biological replicates yielded comparable results. In the 1d samples, Fe_{ppt} had δ^{56}Fe of 0.18 ± 0.06‰ and 0.21 ± 0.05‰ for SW2-2 and SW2-3 respectively, significantly lower than that of the initial substrate Fe(II) with an average δ^{56}Fe of 0.51 ± 0.01‰ (2se, N = 2). As the Fe(II) oxidation proceeded, δ^{56}Fe of Fe_{ppt} increased to 1.78‰ in the 4d samples, significantly higher than that of the initial substrate Fe(II) and then gradually decreased to 1.14–1.17‰ in the 22d samples. δ^{56}Fe of the remaining Fe_{aq} gradually decreased from that of the initial substrate Fe(II) to −2.16‰ and −2.46‰ in the 22d samples. Accordingly, the measured fractionation between Fe_{ppt} and Fe_{aq}, defined as $\Delta^{56}Fe_{ppt\text{-}aq} = \delta^{56}Fe_{ppt} - \delta^{56}Fe_{aq}$, was −0.33‰ to −0.29‰ in the 1d samples, became positive (1.33–1.47‰) in the 4d samples, and then gradually increased to 3.31–3.62‰ in the 22d samples. The isotope composition for the Fe_{H2O} and Fe_{NaAc} fractions, which contained both Fe(II) and Fe(III), resembled neither Fe_{aq} nor Fe_{ppt}. Instead, their δ^{56}Fe values were between the corresponding Fe_{aq} and Fe_{ppt} fractions and showed a roughly decreasing trend over time.

4. DISCUSSION

Highly varied Fe(III)/$\sum Fe_{aq}$ of 14d samples (0.3–48%) and 22d samples (12–24%) among the three independent biological replicates indicated that an abiotic oxidation likely occurred during sequential extraction of different Fe species (see a detailed discussion in Appendix). Fe isotopic compositions of Fe_{H2O}, Fe_{NaAc} and Fe_{ppt} should have not significantly affected by this overprint, however, the $\delta^{56}Fe_{aq}$ for SW2-2 and SW2-3 had to be corrected based on mass balance. Fe isotope fractionation during Fe(II) oxidation by *R. ferrooxidans* SW2 is discussed below with consideration of the potential abiotic oxidation during sampling.

4.1. Fe isotopic composition of Fe_{H2O} and Fe_{NaAc} fractions

Previous studies suggested adsorbed and incorporated Fe species into precipitates as intermediate pools existed in precipitates, such as adsorbed $Fe(II)_{aq}$ (Icopini et al., 2004; Jang et al., 2008; Swanner et al., 2015; Wu et al., 2017). In order to remove these adsorbed and incorporated Fe species from precipitates, and constrain the Fe isotope compositions of intermediates, H_2O and NaAc were used to wash precipitates. Wu et al. (2017) calculated the Fe isotope compositions of intermediates ($Fe(II)_{interm}$ and $Fe(III)_{interm}$) based on mass balance, assuming that Fe_{H2O} and Fe_{NaAc} both consisted of $Fe(II)_{interm}$ and $Fe(III)_{interm}$ and that each intermediate specie had the same isotopic composition. Following equations from Wu et al. (2017) (Eqs. (2) and (3)), the isotopic compositions of $Fe(II)_{interm}$ and $Fe(III)_{interm}$ were calculated for the experiments here (see Table S3).

$$\delta^{56}Fe_{H2O} = \delta^{56}Fe(II)_{interm} \times Fe(II)_{H2O}(\%) + \delta^{56}Fe(III)_{interm} \times Fe(III)_{H2O}(\%) \quad (2)$$

$$\delta^{56}Fe_{NaAc} = \delta^{56}Fe(II)_{interm} \times Fe(II)_{NaAc}(\%) + \delta^{56}Fe(III)_{interm} \times Fe(III)_{NaAc}(\%) \quad (3)$$

where $Fe(II)_{H2O}$ (%), $Fe(III)_{H2O}$ (%), $Fe(II)_{NaAc}$ (%) and $Fe(III)_{NaAc}$ (%) were the ratios between Fe(II) or Fe(III)

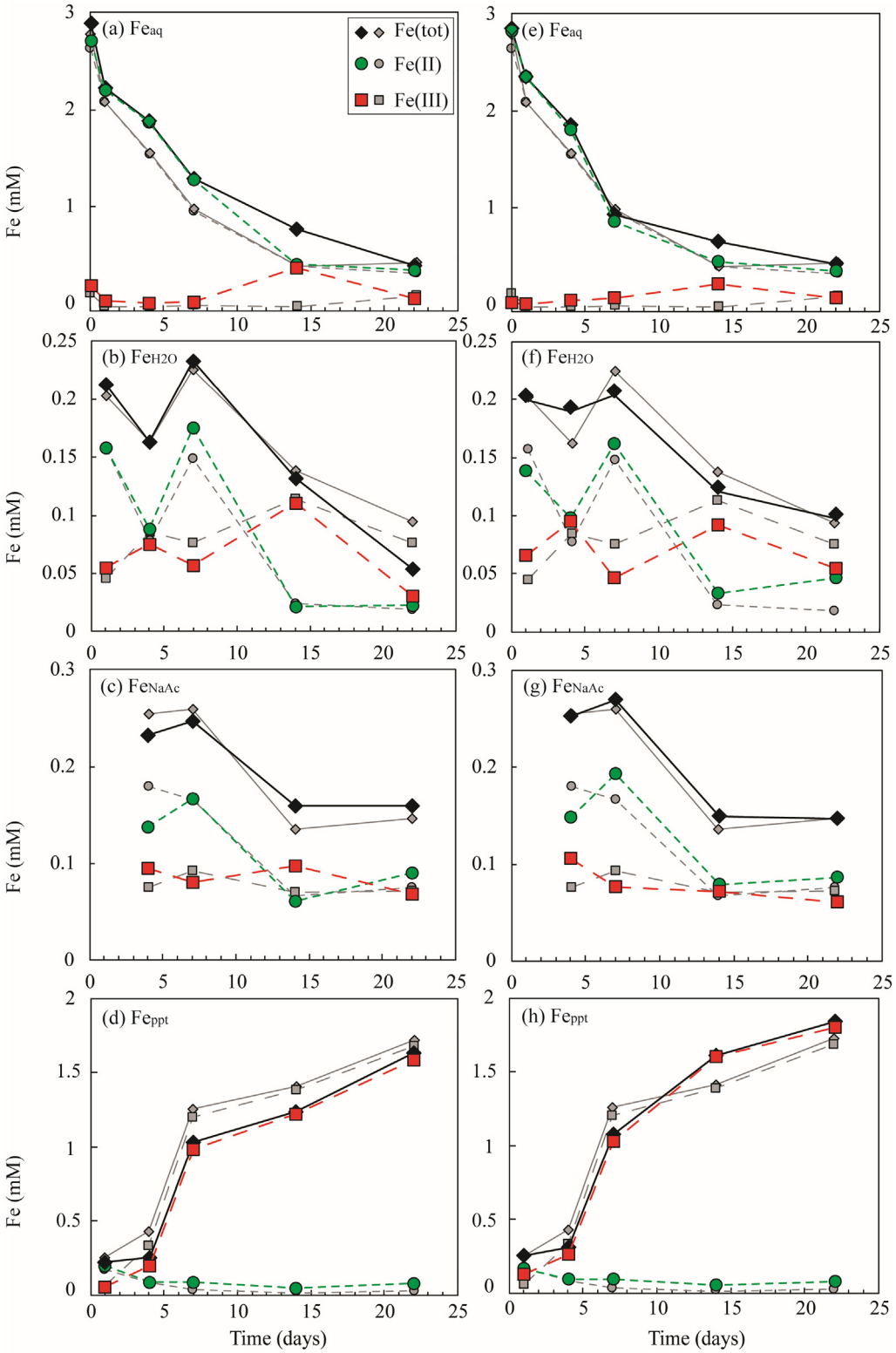

Fig. 3. Fe(II), Fe(III) and total Fe concentration determined for (a) (e) the aqueous Fe fraction (Fe_{aq}), (b) (f) the H_2O-washed fraction (Fe_{H2O}), (c) (g) the NaAc-washed fraction (Fe_{NaAc}) and (d) (h) the precipitated fraction (Fe_{ppt}) at different time points during Fe(II) oxidation by *R. ferrooxidans* SW2. The data shown are from the triplicate runs SW2-1 (a-h, smaller, gray symbols), SW2-2 (a-d, bigger, colored symbols) and SW2-3 (e-h, bigger, colored symbols).

Table 2
Iron isotope compositions of Fe_{aq} and Fe_{ppt} fractions for the biological replicates SW2-2 and SW2-3 measured during Fe(II) oxidation by *R. ferrooxidans* SW2.

Day	ppt rate [a]	Frac. Fe_{ppt} [b]	Fe(III) /∑Fe_{aq} (%)	Fe(III) /∑Fe_{ppt} (%)	$\delta^{56}Fe_{aq}$	2se	$\delta^{56}Fe_{ppt}$	2se	$\delta^{56}Fe_{sys}$ [c]	2se	Measured $\Delta^{56}Fe_{ppt-aq}$	Corrected $\Delta^{56}Fe_{ppt-aq}$
Replicate SW2-2												
0	0.21	0.00	6.4	NA [d]	0.51	0.06	NA	NA	0.51	0.06	NA	NA
1		0.08	1.1	13.0	0.51	0.06	0.18	0.06	0.47	0.06	−0.33	−0.38
4		0.11	0.3	74.0	0.44	0.06	1.78	0.04	0.59	0.05	1.33	1.44
7		0.44	0.8	95.0	−0.41	0.06	1.76	0.06	0.48	0.04	2.17	2.09
14	0.02	0.62	47.7	99.1	−1.38	0.06	1.25	0.06	0.12	0.04	2.63	2.34
22		0.81	11.6	97.0	−2.46	0.06	1.17	0.06	0.41	0.06	3.62	2.90
Replicate SW2-3												
0	0.22	0.00	0.9	NA	0.52	0.03	NA	NA	0.52	0.03	NA	NA
1		0.09	0.2	39.9	0.51	0.03	0.21	0.05	0.47	0.03	−0.29	−0.35
4		0.13	2.4	82.4	0.30	0.03	1.78	0.05	0.52	0.03	1.47	1.47
7		0.53	7.9	95.4	−0.40	0.03	1.65	0.03	0.60	0.03	2.04	2.25
14	0.04	0.71	32.2	99.5	−2.28	0.03	1.22	0.03	0.22	0.04	3.51	2.98
22		0.81	15.9	97.8	−2.16	0.05	1.14	0.05	0.47	0.05	3.31	3.02

[a] precipitation rate (mM/d) is calculated by the increase of total Fe concentration of all Fe_{H2O}, Fe_{NaAc} and Fe_{ppt} fractions along with time.
[b] Frac. $Fe_{ppt} = Fe(tot)_{ppt}/(Fe(tot)_{ppt} + Fe(tot)_{aq})$.
[c] Fe isotope composition of the whole system are calculated by a concentration weighted average for isotope compositions of Fe_{aq}, Fe_{H2O}, Fe_{NaAc} and Fe_{ppt}.
[d] NA = not available.

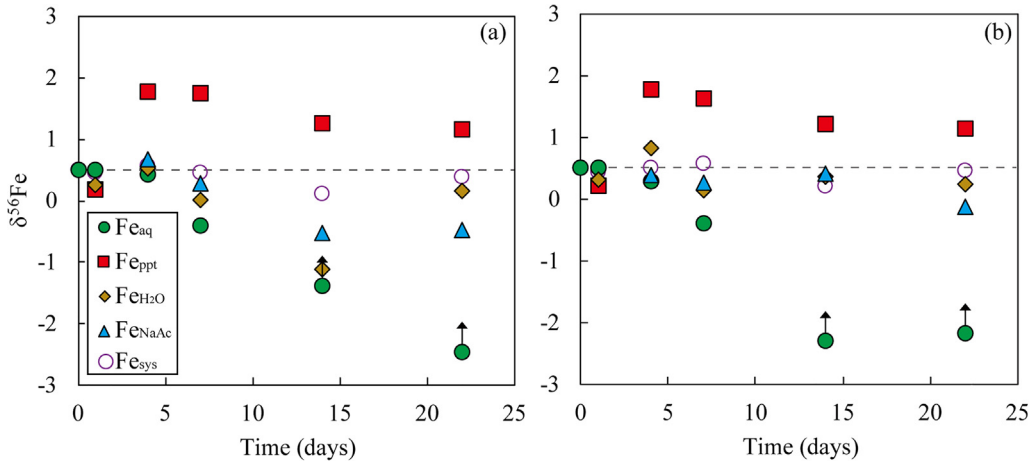

Fig. 4. Measured Fe isotope composition of different Fe fractions: Fe_{aq}, Fe_{H2O}, Fe_{NaAc} and Fe_{ppt} at different time points for the replicate runs (a) SW2-2 and (b) SW2-3. Arrows denote Fe_{aq} at 14d and 22d being affected by an abiotic oxidation during sampling (details described in Appendix). Fe isotope compositions of the whole system ($\delta^{56}Fe_{sys}$) are calculated by a concentration-weighted average for Fe_{aq}, Fe_{H2O}, Fe_{NaAc} and Fe_{ppt} fractions. The dashed lines represent the initial values of $\delta^{56}Fe_{sys}$ for SW2-2 and SW2-3.

concentration and total Fe concentration of H_2O washing fraction and NaAc washing fraction, respectively. The results showed there was a significant difference in the isotopic composition between $Fe(III)_{interm}$ and $Fe(III)_{ppt}$, in contrast to the results in Wu et al. (2017), in which most of $\delta^{56}Fe$ values for $Fe(III)_{interm}$ were nearly the same as the $Fe(III)_{ppt}$. Here we attributed this difference to the difficulty to obtain accurate Fe(III)/∑Fe of Fe_{H2O} and Fe_{NaAc} fractions. As discussed on the abiotic oxidation during sequential extraction of different Fe species in Appendix, an abiotic oxidation may have occurred during sampling and concentration measurement, especially for aqueous solutions with low Fe(II) concentrations. Fe_{H2O} and Fe_{NaAc} fractions had Fe concentrations (<0.27 mM), lower than those of Fe_{aq} at 14d and 22d (0.61 mM and 0.42 mM, respectively). Fe(III)/Fe(II) ratios in Fe_{H2O} and Fe_{NaAc} fractions may thus be overestimated, resulting in erroneous calculated isotopic compositions of $Fe(II)_{interm}$ and $Fe(III)_{interm}$. Therefore, we would discard discussions about the intermediate Fe pool and focus on the fractionation between $Fe(II)_{aq}$ and the washed precipitates. Previous studies suggested that intermediate Fe species can be washed by two steps leaching of H_2O and NaAc without significant change in isotope composition of precipitates (Crosby et al., 2005, 2007; Swanner et al., 2015).

4.2. Isotopic fractionation between precipitates and Fe(II)$_{aq}$

Since there could be an abiotic oxidation of Fe_{aq} during sequential extraction of different Fe species (discussed in detail in Appendix), the $\delta^{56}Fe_{aq}$ for SW2-2 and SW2-3 were corrected based on mass balance using the following equations:

$$\delta^{56}Fe_{aq'} = (\delta^{56}Fe_{sys(t=0)} - \delta^{56}Fe_{H2O} \times F_{H2O} - \delta^{56}Fe_{NaAc} \times F_{NaAc} - \delta^{56}Fe_{ppt} \times F_{ppt}) / (1 - F_{H2O} - F_{NaAc} - F_{ppt}) \quad (4)$$

where $\delta^{56}Fe_{sys(t=0)}$ is ^{56}Fe isotope composition of the initial whole system, $\delta^{56}Fe_{H2O}$, $\delta^{56}Fe_{NaAc}$ and $\delta^{56}Fe_{ppt}$ are ^{56}Fe isotope composition of each fraction for SW2-2 and SW2-3. The fraction of H_2O, NaAc and precipitation (F_{H2O}, F_{NaAc} and F_{ppt}) of SW2-1 are used in Eq. (4) to correct $\delta^{56}Fe_{aq}$ for SW2-2 and SW2-3 due to the relatively lower Fe(III)/$\sum$Fe$_{aq}$ (e.g. 0.3% in 14d) of SW2-1 than that of SW2-2 (e.g. 48% in 14d) and SW2-3 (e.g. 32% in 14d). Data of corrected $\delta^{56}Fe_{aq}$ ($\delta^{56}Fe_{aq'}$) is shown in Table S4. The corrected Fe isotope fractionation between precipitates and Fe(II)$_{aq}$ ($\Delta^{56}Fe_{ppt-aq'}$) for two biological replicates changed from negative (-0.37 ± 0.04‰) after 1 day cultivation to positive (1.46 ± 0.04‰) at 4d, and kept increasing until 2.96 ± 0.17‰ after 22 days of cultivation (Table 2). The change in $\Delta^{56}Fe_{ppt-aq'}$ corresponded to the decrease of Fe(II)/Fe$_{ppt}$, implying a simultaneous change of mineral species, i.e. from a mixture of Fe(II) species and Fe(III) species to only Fe(III) species, in precipitates. Both changes of $\Delta^{56}Fe_{ppt-aq'}$ and mineral species suggested the Fe isotopic fractionation here can not be explained, neither by a simple equilibrium nor Rayleigh fractionation process. The δ^{56}-Fe$_{ppt}$ and $\delta^{56}Fe_{aq'}$ were compared with equilibrium and Rayleigh fractionation processes in Fig. 5. Rayleigh fractionation was calculated using the following equation:

$$\delta^{56}Fe_{aq} = \delta^{56}Fe_{initial} + \Delta^{56}Fe_{ppt-aq} \times \ln(1 - F_{ppt}) \quad (5)$$

where F_{ppt} is Fraction. $Fe_{ppt} = Fe_{ppt}/(Fe_{ppt} + Fe_{aq})$ considering that Fe_{aq} and Fe_{ppt} were dominant in the system. A mass of fractionation factors for Rayleigh were chosen to fit the $\delta^{56}Fe_{ppt}$ and $\delta^{56}Fe_{aq'}$ values (some of them, i.e., 0.3‰, 1.4‰ and 2.96‰, were illustrated in Fig. 5); however, there was no factor that could fit exactly all $\delta^{56}Fe_{ppt}$ and $\delta^{56}Fe_{aq'}$ values.

The variation of Fe isotope fractionation factors here might be induced by a change of iron species during Fe (II) oxidation. To evaluate the effect of changing Fe species, the equilibrium isotope fractionation factors between Fe_{ppt} and Fe_{aq} are calculated following Eqs. (6)–(8) based on 1000lnβ ($\beta = {}^{56}Fe/{}^{54}Fe$ reduced partition function ratio relative to a dissociated Fe atom) available in the literatures.

$$\Delta^{56}Fe_{ppt-aq,\,(calculated)} = 1000\ln\beta_{ppt} - 1000\ln\beta_{aq} \quad (6)$$

$$1000\ln\beta_{aq} = \sum_{i=1}^{n} f_{n(aq)} \times 1000\ln\beta_{n(aq)} \quad (7)$$

$$1000\ln\beta_{ppt} = \sum_{i=1}^{n} f_{n(ppt)} \times 1000\ln\beta_{n(ppt)} \quad (8)$$

where f is the fraction and n is the number of Fe_{aq} species or Fe_{ppt} species. In general, β-values reflect differences in the vibrational frequencies between two different isotopes of the same element in a molecule. Vibrational frequencies can be measured by a variety of spectroscopic methods, such as Raman, infrared, Mössbauer spectroscopy and inelastic neutron scattering spectrum. First-principles electronic structure calculations are also used to constrain β-values, such as Density Functional Theory (DFT). DFT calculates electronic energies from electron densities to constrain β-values, which is better suited for molecules containing transition elements (e.g., Schauble 2004). Experimental methods including the three-isotope method, reversed isotope exchange experiments, partial exchange method and synthesis methods were developed to evaluate Fe isotope fractionation factors. A review of theoretical and experimental methods to constrain Fe isotope fractionations was presented in chapter 3 of Johnson et al. (2020).

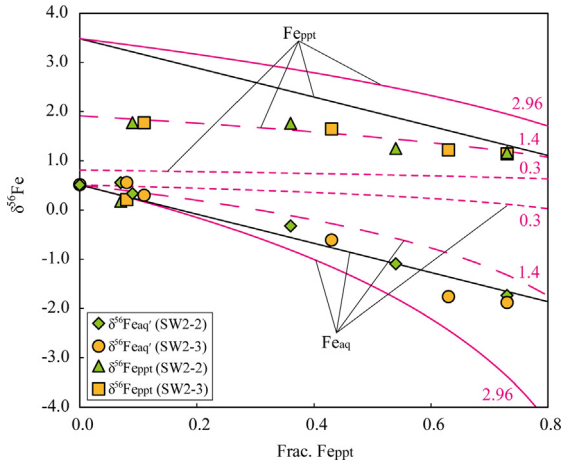

Fig. 5. The $\delta^{56}Fe_{ppt}$ and $\delta^{56}Fe_{aq'}$ for runs SW2-2 and SW2-3 in comparison to the Rayleigh fractionation (pink lines) and equilibrium fractionation (black lines) processes. Curves with variable fractionation factors, 0.3‰, 1.4‰ and 2.96‰ for Rayleigh (arbitrarily selected) and 2.96 ± 0.17‰ for equilibrium fractionation (this study), are shown. (For interpretation of the references to colour in this figure legend, the reader is referred to the web version of this article.)

In this study, the Fe_{aq} species in medium were calculated using Geochemists Workbench 12.0. The results showed Fe_{aq} species were $Fe(H_2O)_6^{2+}$ (76.7%), $FeHCO_3^+$ (15.6%), $FeSO_{4aq}$ (5.1%), $FeCO_{3aq}$ (1.5%), $FeCl^+$ (0.9%), and $FeOH^+$ (0.2%). Although the measured Fe(III)/$\sum$Fe$_{aq}$ values for 14d samples and 22d samples were higher, this could be an artifact due to the abiotic oxidation during sampling as discussed in Appendix. The 1000lnβ-values calculated and summarized in Rustad et al. (2010) and Fujii et al. (2014) were adopted here for main Fe specie $Fe(H_2O)_6^{2+}$ (4.81) and minor Fe species $FeHCO_3^+$ (5.43), $FeSO_{4aq}$ (5.56), $FeCO_{3aq}$ (5.99), $FeCl^+$ (5.02), and $FeOH^+$ (5.66) at 20 °C.

Whereas for precipitates, a change of iron species can make a substantial difference on the accumulative 1000lnβ. Fe(II)/$\sum$Fe$_{ppt}$ in the 1d sample was as high as ~60% to 87%, partially owing to that the precipitates in 1d were not washed by NaAc. Given the Fe(II) was saturated initially, the Fe(II) species in precipitates for 1d

sample were inferred to be $Fe(OH)_2$, $FeCO_3$ and $Fe_3(PO_4)_2$ which co-precipitated with oxidation products during Fe (II) oxidation. Since $Fe(II)/\sum Fe_{ppt}$ was close to zero (~0.5–2%), ferrihydrite could be the only dominant mineral in the precipitates from 7d to 22d. The $1000\ln\beta$-value (8.03 at 20 °C) for ferrihydrite was obtained based on the experimental results determined for hexaquo Fe^{2+} and the ferric oxide in chapter 3 of Johnson et al. (2020). However, so far, there is no constraint on $1000\ln\beta$ for $Fe(OH)_2$ and $Fe_3(PO_4)_2$ in previous studies. In addition, the proportion of $Fe(OH)_2$, $FeCO_3$ and $Fe_3(PO_4)_2$ in the precipitates for 1d samples are not clear. Therefore, we only used $1000\ln\beta$ of siderite ($FeCO_3$) for $Fe(II)_{ppt}$ in the precipitates. The adopted $1000\ln\beta$-value for siderite (~4.32 at 20 °C) was the average of the Mössbauer-derived $1000\ln\beta$-value reported in Polyakov and Mineev (2000) and the DFT-derived $1000\ln\beta$-value of Blanchard et al. (2009). The consistency between experimental and theoretical fractionation factors based on previous literatures was shown in Fig. S4. Calculated fractionation factors were given in Table S4. The equilibrium $\Delta^{56}Fe_{ppt\text{-}aq}$ was then compared with the corrected ones in Fig. S5. Corrected factors were obviously lower than calculated factors for 1d to 7d harvest, which indicated that kinetic effects should have played a role in the rapid precipitation during the first 7d-incubation. While corrected $\Delta^{56}Fe_{ppt\text{-}aq'}$ (2.96 ± 0.17‰) in 22d was perfectly consistent with the calculated equilibrium fractionation factor (2.97 ± 0.04‰), implying that the Fe isotope fractionation between Fe_{aq} and Fe_{ppt} could have been reached to complete or near-complete equilibrium.

Previous Fe(II) oxidation experiments using anoxygenic photosynthetic microorganisms and acidophilic Fe(II)-oxidizing bacteria were thought to reflect an equilibrium fractionation between aqueous Fe^{2+} and aqueous Fe^{3+} followed by a kinetic fractionation associated with the precipitation of solid ferric (oxyhydr)oxides from the aqueous Fe^{3+}, resulting in final fractionation factors ranging from 0.96‰ to 3.1‰ (Croal et al., 2004; Balci et al., 2006; Swanner et al., 2015, 2017; Wu et al., 2017). Fe isotope fractionation factors at room temperature between $Fe(II)_{aq}$ and $Fe(III)_{aq}$ or Fe(III) (oxyhydr)oxides produced either abiotically or via Fe(II)-oxidizing bacteria were summarized in Table S5. Microbially mediated equilibrium fractionation similar to our results has been previously observed in nitrate-reducing Fe(II) oxidation, in which equilibrium fractionation between ferric (oxyhydr)oxides products and $Fe(II)_{aq}$ (3.0‰) was reached within 21 days (Kappler et al., 2010). The fractionation factors from the present study and those from Kappler et al. (2010) were also consistent with that inferred by abiotic isotope exchange experiments (~3.2‰) (Wu et al., 2011). Johnson et al. (2020) have divided iron-oxidizing experiments using bacteria into three broad Fe oxidation rates based on the number of days it took to reach 50% oxidation. The intermediate rate was referred to that 50% Fe(II) oxidation occurred within 9 to 19 days, in which the $\Delta^{56}Fe_{Fe(III)\text{–ferric oxide}}$ was positive and varied from 1.5 to 0.2‰, depending on precipitation rates and the mineralogy of the Fe(III) (oxyhydr)oxides (Balci et al. 2006; Skulan et al. 2002). Following the classification method in Johnson et al. (2020), oxidation rates in both Kappler et al. (2010) and here were intermediate. It is speculated that Fe(II) oxidation and precipitation of Fe(III) (oxyhydr)oxides occurring in the periplasm maintained equilibrium isotope exchange between Fe^{2+} and the precipitates (Kappler et al. 2010). Although there is no study showing that Fe(II) oxidation and precipitation of Fe(III) (oxyhydr)oxides occurs in the periplasm of strain SW2, compared with the relatively higher precipitation rate (0.23 ± 0.02 mM day^{-1}) in the first 7 days (as shown in Fig. 6), the precipitation rate decreased to 0.02 ± 0.01 m M day^{-1} in the last 15 days, which could promote isotopic equilibrium between precipitates and $Fe(II)_{aq}$, and even compensated the fractionation caused by the early kinetic effect. Therefore, at the end of experiments, the Fe isotope fractionation between ferrihydrite and $Fe(II)_{aq}$ approached a value of 2.96 ± 0.17‰ (2se, N = 2) that is expected for complete or near-complete equilibrium (Fig. S5).

The experiments here thus illustrated a fractionation progress of Fe isotope from disequilibrium to complete or near-complete equilibrium between precipitates and $Fe(II)_{aq}$ during 22-days cultivation of anoxygenic phototrophic Fe(II)-oxidizer *R. ferrooxidans* SW2. The change of Fe isotope fractionation from disequilibrium to complete or near-complete equilibrium depended on the competition between a kinetic effect and isotope exchange. In first 7 days, a kinetic effect upon rapid Fe(II) oxidation was dominating in the competition, resulting in a disequilibrium fractionation. While Fe(II) oxidation rate decreased to 0.02 ± 0.01 mM day^{-1} in the last 15 days, isotope exchange overwhelmed the kinetic effect, promoting a final isotope equilibrium between ferrihydrite and $Fe(II)_{aq}$. The high surface-to-volume ratio of small size nanoparticles of ferrihydrite here could facilitate isotope exchange. The exact size of the final oxidation products, i.e. ferrihydrite, was not determined but can be estimated to be <10 nm based on TEM results, which was similar with the ferrihydrite synthesized at room temperature of ~2–3 nm (Liu et al., 2005; Wu et al., 2011; Posth et al., 2013). Another process to promote isotope exchange was the dissolution-oxidation-reprecipitation of ferrous minerals, i.e., ferrous minerals co-precipitated with oxidation products in the first day, subsequently dissolved and oxidized by SW2, and finally reprecipitated as ferrihydrite. In summary, the low oxidation rate, small size of ferrihydrite and dissolution-oxidation-reprecipitation process most likely promoted isotope exchange overwhelming the earlier kinetic effect. Note that isotopic equilibrium between aqueous solution and instantaneous precipitates must have been reached before the end of the 22-days experiment, likely since the 7 days when the oxidation rate dropped to 0.02 ± 0.01 mM day^{-1} (Fig. 6), because it took time to erase the earlier kinetic signals in accumulative precipitates via isotopic exchange.

4.3. Implications for tracing biogeochemical Fe cycling on early Earth

Previous studies have shown that the Archean and Paleoproterozoic oceans were anoxic and ferruginous (Cloud, 1973; Holland, 1984). The presence of both ferric and ferrous minerals gave IFs an average oxidation state of

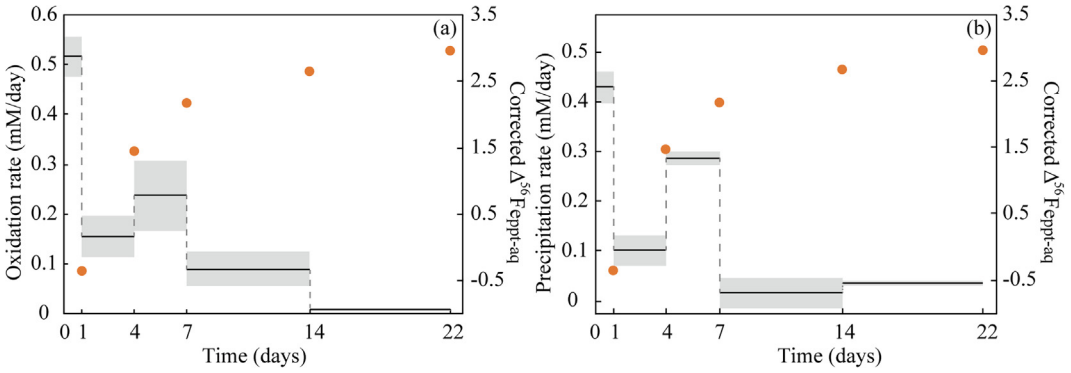

Fig. 6. The average oxidation rates (a) and precipitation rates (b) for triplicates (SW2-1, SW2-2 and SW2-3) from 0 day to 22 day. The black lines and grey areas correspond to the average oxidation/precipitation rates and errors for triplicates. The oxidation rates are calculated by the decrease of Fe(II) concentration of Fe_{aq} fraction along with time. The precipitation rates are calculated by the increase of total Fe concentration of Fe_{H2O}, Fe_{NaAc} and Fe_{ppt} fractions along with time. The orange circles refer to the average values of corrected Fe isotope fractionation factors for SW2-2 and SW2-3. (For interpretation of the references to colour in this figure legend, the reader is referred to the web version of this article.)

$Fe^{2.4+}$, indicating that there was an oxidization mechanism converting Fe^{2+}_{aq} to Fe^{3+} (Klein and Beukes, 1992; Konhauser et al., 2017). Based on molecular phylogenetic evidence, Fe(II) oxidation rates by anoxygenic photosynthetic bacteria and chemical analyses from IFs, anoxygenic photosynthesis have possibly played a prominent role in IFs deposition (Konhauser et al., 2002; Kappler et al., 2005; Xiong, 2007). Both freshwater and marine strains could oxidize Fe^{2+}_{aq} to Fe(III) (oxyhydr)oxides, e.g. ferrihydrite, that was consistent with the most likely precursor IFs minerals (Kappler and Newman, 2004; Wu et al., 2017). Previous studies also illustrated freshwater strains behaved similarly as the marine strains in many aspects such as Fe(II) oxidation rates and cell-mineral interactions. The Fe(II) oxidation rate by the marine Fe(II)-oxidizing phototroph *Rhodovulum iodosum* was reported as 0.3 mM day^{-1} (Schad et al., 2019), which was consistent with the values observed for SW2 at a similar light intensity in previous studies (Kappler et al., 2005; Hegler et al., 2008) and here. TEM and CLSM (confocal laser scanning microscope) images showed both freshwater and marine photoferrotrophs cells were not covered completely by the Fe(III) precipitates and had similar strategies to avoid encrustation. For example, they can excrete fibers or EPS binding Fe(III) and inducing precipitates away from cell surfaces, implying a similar cell-mineral interaction of freshwater and marine photoferrotrophs (Miot et al., 2009a; Wu et al., 2014). Similar with the freshwater photoferrotroph in this study, the equilibrium fractionation between Fe (III) (oxyhydr)oxides produced by marine photoferrotrophs and $Fe(II)_{aq}$ could be approached.

The dissolved Fe(II) concentration in the pre-GOE oceans ranged from 0.03 to 0.5 mM (Holland, 1973; Morris, 1993), which was lower than the initial Fe(II) concentration in this study (~2.7 mM). Kappler et al. (2005) have explained the Fe(III) inventories in IFs with a 0.014 mM/day Fe(II) oxidation rate of anoxygenic photoferrotrophy which was lower than the Fe(II) oxidation rate of 0.02 mM/day after 7 days in this study. A previous study has shown that the Fe(II) oxidation rate of *Rhodobacter ferrooxidans* SW2 would decrease as the initial Fe(II) concentration decreased from 8 mM to 0.2 mM (Hegler et al., 2008). Therefore, it is conservative to estimate that the Fe (II) oxidation rate of anoxygenic photoferrotrophy in Archean oceans was likely lower than that in this study. Additionally, ultrafine crystal hematite, which can be transformed from ferrihydrite through dehydration, in banded IFs was 3–5 nm in size (Ahn and Buseck, 1990; Chan et al., 2013), which was similar in size to the biogenic ferrihydrite precipitated in this study. On the basis of SEM observations, Li (2014) hypothesized that the nanobands of fine-grained hematite in three sets of IFs (Kuruman Iron Formation, South Africa; Brockman Iron Formation, Western Australia; Abitibi Greenstone Belt, Canada) represented possible diurnal depositions with a precipitation rate of 26 nm/day. By contrast, U-Pb dating suggested that the banded IFs from the Hamersley Group may have been deposited at a rate as fast as 100–1000 m/m.y (<2 μm/day) (Barley et al., 1997). Consistent with Kappler et al. (2010), this study suggested that the biogenic ferric (oxyhydr)oxides could approach isotope equilibrium with $Fe(II)_{aq}$ in only ~20 days. Even taking the fastest precipitation rate of Fe(III) minerals for IFs in estimate, infiltration of the fluids into a depth of <40 μm through inter-particle pores was sufficient to keep Fe isotope equilibrium between Fe(III) (oxyhydr)oxides and ferrous Fe pools. Although Archean seawater was high (or even saturated) in dissolved Si, and the presence of Si in seawater may hinder isotope exchange between ferrihydrite and $Fe(II)_{aq}$ (Wu et al., 2011, 2012), the lower oxidation rate and redox-driven electron exchange during Fe(II) oxidation by anoxygenic photoferrotrophy could facilitate the isotope exchange between Fe (II) and ferrihydrite. Therefore, here we illustrate that the ferrihydrite produced by Fe(II) oxidation by anoxygenic photoferrotrophy could reach Fe isotope equilibrium with aqueous solution within few to 22 days. This is very important for allowing explanation of Fe isotopic data for Archean IFs without fear that each specific system was

dominated by its own unique and difficult to predict kinetic effects.

Available $\delta^{56}Fe$ data for bulk IFs as well as their magnetite and hematite separates are compiled in Fig. 7(a). $\delta^{56}Fe$ for a quite number of IFs samples with variable ages are lower than that of the source of aqueous Fe(II) from hydrothermal fluids (~0‰) (Yamaguchi et al., 2005; Johnson et al., 2008b; Li et al., 2013). These negative $\delta^{56}Fe$ of IFs samples could be attributed to local contribution of Fe(II) with light Fe isotope composition from the continental shelfs, evidenced by $\delta^{56}Fe$ decreasing with $\varepsilon_{Nd}(t)$ values in the Dales Gorge member (~2.5 Ga) BIFs (Li et al., 2015). Since few studies have reported Fe isotope data with $\varepsilon_{Nd}(t)$ values for IFs samples, the extent to which continental components contribute to the Fe(II) source for IFs remains unclear. Alternatively, despite the instantaneous precipitates were in isotope equilibrium with the fluids, precipitation of IFs was largely a Rayleigh process. This is reasonable considering that the precipitates would be isolated from the fluids by subsequent burial and compaction. Therefore, we calculated Fe oxidized fraction of the water columns from which IFs were precipitated by a Rayleigh fractionation model:

$$\delta^{56}Fe_{aq} = \delta^{56}Fe_{initial} + \Delta^{56}Fe_{ppt-aq'} \times \ln(1 - F_{oxidized}) \quad (9)$$

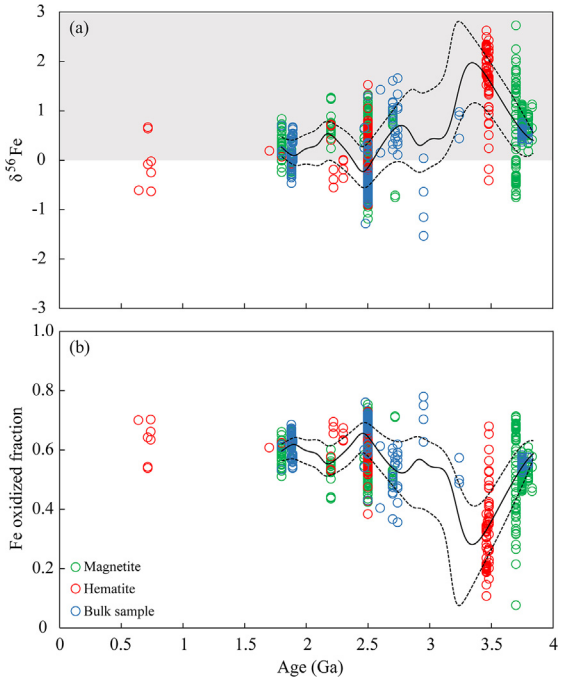

Fig. 7. Secular $\delta^{56}Fe$ variations of IFs (a). Data are compiled from the literatures and more details are provided in Table S7. Only magnetite, hematite and bulk samples with Fe dominantly in magnetite and hematite are shown. Fe oxidized fraction of the water column where IFs precipitated (b) is calculated using a Rayleigh model. The grey area in (a) refers to the $\delta^{56}Fe$ range of Fe (III) oxides precipitates if they always keep isotope equilibrium with the fluid and the system has an initial $\delta^{56}Fe \sim 0‰$. The solid and dashed curves represent moving average (LOESS) of the full, top half and bottom half data respectively.

$$\delta^{56}Fe_{ppt} = \delta^{56}Fe_{aq} + \Delta^{56}Fe_{ppt-aq'} \quad (10)$$

$\Delta^{56}Fe_{ppt-aq'}$ (2.96‰) observed here for the anoxygenic phototrophic Fe(II)-oxidizer is adopted, and $\delta^{56}Fe_{initial}$ is assumed to be 0‰, which is the same as that of hydrothermal fluids. The calculation results are shown in Fig. 7(b), and three intriguing insights can be drawn:

(i) A very low Fe oxidized fraction (i.e., <25%) has only be observed before 3.4 Ga, suggesting that highly reducing shallow water columns may have disappeared after 3.4 Ga. A whiff of oxygen before the GOE has been supported by many evidences of elements and isotopic systems (Mo, Re, S, N, Fe, Mo, U, Os, Se, Th, Hg) from the sediments before 2.45 Ga (Anbar et al., 2007; Koehler et al., 2018; Slotznick et al., 2022).

(ii) Some >3.4 Ga IFs have low $\delta^{56}Fe$ down to −0.7‰, indicating a high Fe oxidized fraction of the water column up to 71%. Oxidization of >3.4 Ga oceans to such extent seems unlikely. These IFs may have been precipitated in shallow restricted basins, where early flourishing of anoxygenic photosynthesis likely occurred due to the relatively high nutrient abundance (Johnson et al., 2022).

(iii) Despite the GOE, a partial oxidized paleo-ocean continued till the Neoproterozoic, which is also evidenced by the manganiferous bands and the speciation of Fe in Neoproterozoic sediments (Holland, 2006; Canfield et al., 2008; Spinks et al., 2018).

5. CONCLUSIONS

The Fe isotope fractionation between precipitates produced by anoxygenic phototrophic Fe(II)-oxidizer *Rhodobacter ferrooxidans* SW2 and $Fe(II)_{aq}$ ($\Delta^{56}Fe_{ppt-aq'}$) changed from negative (ca. −0.37‰) after 1 day cultivation to positive (ca. 1.46‰) at 4 days, and kept increasing until 2.96‰ after 22 days of cultivation. The corrected $\Delta^{56}Fe_{ppt-aq'}$ (2.96 ± 0.17‰) in 22d was perfectly consistent with the calculated equilibrium fractionation factor (2.97 ± 0.04‰), implying that the Fe isotope fractionation between Fe_{aq} and Fe_{ppt} could have been reached to complete or near-complete equilibrium. The change of Fe isotope fractionation from disequilibrium to complete or near-complete equilibrium indicated a competition between the kinetic effect and isotope exchange. The final equilibrium may have been promoted by continuous coupled exchange of Fe ions and electrons between co-existing $Fe(II)_{aq}$ and Fe(III) precipitates. Combined with estimates on the oxidation and precipitation rates of Fe(III) minerals in ancient oceans, this study highlights the Fe isotope composition of these Fe(III) (oxyhydr)oxides has been in equilibrium with the fluids from which they precipitated, i.e. in some cases solely from seawater and thus can reflect the geochemical and redox state of Archean and Paleoproterozoic oceans to a certain extent.

Declaration of Competing Interest

The authors declare that they have no known competing financial interests or personal relationships that could have appeared to influence the work reported in this paper.

ACKNOWLEDGEMENTS

We would like to thank Wenning Lu for assistance in MC-ICP-MS analysis, Wenfang Wu and Fuxian Wang for help with culturing of *Rhodobacter ferrooxidans* SW2, Xu Tang and Lixin Gu for assistance in SEM and TEM analyses, Xiangxian Ma for Mössbauer spectroscopic analysis. This work was supported by National Natural Science Foundation of China (41621004, 41890843, 41502320), China Postdoctoral Science Foundation (2021M693151), Fundamental Research Funds for the Central Universities (3-7-5-2019-07), the 111 Project of the Ministry of Science and Technology, China (No. BP0719021), and the State Key Laboratory of Geological Processes and Mineral Resources.

APPENDIX A. SUPPLEMENTARY MATERIAL

Supplementary material to this article can be found online at https://doi.org/10.1016/j.gca.2022.06.034.

REFERENCES

Ahn J. H. and Buseck P. R. (1990) Hematite nanospheres of possible colloidal origin from a precambrian banded iron formation. *Science* **250**, 111–113.

Anbar A. D., Duan Y., Lyons T. W., Arnold G. L., Kendall B., Creaser R. A., Kaufman A. J., Gordon G. W., Scott C., Garvin J. and Buick R. (2007) A whiff of oxygen before the great oxidation event? *Science* **317**, 1903.

Balci N., Bullen T. D., Witte-Lien K., Shanks W. C., Motelica M. and Mandernack K. W. (2006) Iron isotope fractionation during microbially stimulated Fe(II) oxidation and Fe(III) precipitation. *Geochim. Cosmochim. Acta* **70**, 622–639.

Barley M. E., Pickard A. L. and Sylvester P. J. (1997) Emplacement of a large igneous province as a possible cause of banded iron formation 2.45 billion years ago. *Nature* **385**, 55–58.

Beard B. L., Johnson C. M., Cox L., Sun H., Nealson K. H. and Aguilar C. (1999) Iron Isotope Biosignatures. *Science* **285**, 1889–1892.

Beard B. L., Handler R. M., Scherer M. M., Wu L., Czaja A. D., Heimann A. and Johnson C. M. (2010) Iron isotope fractionation between aqueous ferrous iron and goethite. *Earth Planet. Sci. Lett.* **295**, 241–250.

Blanchard M., Poitrasson F., Méheut M., Lazzeri M., Mauri F. and Balan E. (2009) Iron isotope fractionation between pyrite (FeS2), hematite (Fe2O3) and siderite (FeCO3): A first-principles density functional theory study. *Geochim. Cosmochim. Acta* **73**(21), 6565–6578.

Canfield D. E., Poulton S. W., Knoll A. H., Narbonne G. M., Ross G., Goldberg T. and Strauss H. (2008) Ferruginous Conditions Dominated Later Neoproterozoic Deep-Water Chemistry. *Science* **321**, 949–952.

Chan L. S., Li Y.-L., Cole D. R. and Konhauser K. (2013) Quartz nanocrystals in the 2.48 Ga Dales Gorge banded iron formation of Hamersley, Western Australia: Evidence for a change from submarine to subaerial volcanism at the end of the Archean. *Am. Miner.* **98**, 582–587.

Chen K.-Y., Yuan H.-L., Liang P., Bao Z.-A. and Chen L. (2017) Improved nickel-corrected isotopic analysis of iron using high-resolution multi-collector inductively coupled plasma mass spectrometry. *Int. J. Mass Spectrom.* **421**, 196–203.

Cloud P. (1973) Paleoecological significance of the banded iron-formation. *Econ. Geol.* **68**, 1135–1143.

Craddock P. R. and Dauphas N. (2011) Iron isotopic compositions of geological reference materials and chondrites. *Geostand. Geoanal. Res.* **35**, 101–123.

Croal L. R., Johnson C. M., Beard B. L. and Newman D. K. (2004) Iron isotope fractionation by Fe(II)-oxidizing photoautotrophic bacteria 1. *Geochim. Cosmochim. Acta* **68**, 1227–1242.

Crosby H. A., Johnson C. M., Roden E. E. and Beard B. L. (2005) Coupled Fe(II)−Fe(III) electron and atom exchange as a mechanism for Fe isotope fractionation during dissimilatory iron oxide reduction. *Environ. Sci. Technol.* **39**, 6698–6704.

Crosby H. A., Roden E. E., Johnson C. M. and Beard B. L. (2007) The mechanisms of iron isotope fractionation produced during dissimilatory Fe(III) reduction by Shewanella putrefaciens and Geobacter sulfurreducens. *Geobiology* **5**, 169–189.

Dauphas N., Pourmand A. and Teng F.-Z. (2009) Routine isotopic analysis of iron by HR-MC-ICPMS: how precise and how accurate? *Chem. Geol.* **267**, 175–184.

Ehrenreich A. and Widdel F. (1994) Anaerobic oxidation of ferrous iron by purple bacteria, a new type of phototrophic metabolism. *Appl. Environ. Microbiol.* **60**, 4517–4526.

Eickhoff M., Obst M., Schröder C., Hitchcock A. P., Tyliszczak T., Martinez R. E., Robbins L. J., Konhauser K. O. and Kappler A. (2014) Nickel partitioning in biogenic and abiogenic ferrihydrite: The influence of silica and implications for ancient environments. *Geochim. Cosmochim. Acta* **140**, 65–79.

Frierdich A. J., Beard B. L., Reddy T. R., Scherer M. M. and Johnson C. M. (2014) Iron isotope fractionation between aqueous Fe(II) and goethite revisited: New insights based on a multi-direction approach to equilibrium and isotopic exchange rate modification. *Geochim. Cosmochim. Acta* **139**, 383–398.

Frierdich A. J., Nebel O., Beard B. L. and Johnson C. M. (2019) Iron isotope exchange and fractionation between hematite (α-Fe2O3) and aqueous Fe(II): a combined three-isotope and reversal-approach to equilibrium study. *Geochim. Cosmochim. Acta* **245**, 207–221.

Fujii T., Moynier F., Blichert-Toft J. and Albarède F. (2014) Density functional theory estimation of isotope fractionation of Fe, Ni, Cu, and Zn among species relevant to geochemical and biological environments. *Geochim. Cosmochim. Acta* **140**, 553–576.

Garrels R. M., Perry E. A. and Mackenzie F. T. (1973) Genesis of Precambrian iron-formations and the development of atmospheric oxygen. *Econ. Geol.* **68**, 1173–1179.

He Y., Ke S., Teng F. Z., Wang T., Wu H., Lu Y. and Li S. (2015) High-precision iron isotope analysis of geological reference materials by high-resolution MC-ICP-MS. *Geostand. Geoanal. Res.* **39**, 341–356.

Hegler F., Posth N. R., Jiang J. and Kappler A. (2008) Physiology of phototrophic iron (II)-oxidizing bacteria: implications for modern and ancient environments. *FEMS Microbiol. Ecol.* **66**, 250–260.

Hegler F., Schmidt C., Schwarz H. and Kappler A. (2010) Does a low-pH microenvironment around phototrophic FeII-oxidizing bacteria prevent cell encrustation by FeIII minerals? *FEMS Microbiol. Ecol.* **74**, 592–600.

Hohmann C., Winkler E., Morin G. and Kappler A. (2010) Anaerobic Fe(II)-oxidizing bacteria show as resistance and immobilize As during Fe(III) mineral precipitation. *Environ. Sci. Technol.* **44**, 94–101.

Holland H. D. (1973) The oceans: a possible source of iron in iron-formations. *Econ. Geol.* **68**, 1169–1172.
Holland H. D. (1984) The Chemical Evolution of the Atmosphere and Oceans. Princeton University Press.
Holland H. D. (2006) The oxygenation of the atmosphere and oceans. *Philos. Trans. R. Soc. B: Biol. Sci.* **361**, 903–915.
Icopini G. A., Anbar A. D., Ruebush S. S., Tien M. and Brantley S. L. (2004) Iron isotope fractionation during microbial reduction of iron: the importance of adsorption. *Geology* **32**, 205–208.
Jang J.-H., Mathur R., Liermann L. J., Ruebush S. and Brantley S. L. (2008) An iron isotope signature related to electron transfer between aqueous ferrous iron and goethite. *Chem. Geol.* **250**, 40–48.
Johnson C. M., Skulan J. L., Beard B. L., Sun H., Nealson K. H. and Braterman P. S. (2002) Isotopic fractionation between Fe (III) and Fe(II) in aqueous solutions. *Earth Planet. Sci. Lett.* **195**, 141–153.
Johnson C. M., Beard B. L., Klein C., Beukes N. J. and Roden E. E. (2008a) Iron isotopes constrain biologic and abiologic processes in banded iron formation genesis. *Geochim. Cosmochim. Acta* **72**, 151–169.
Johnson C. M., Beard B. L. and Roden E. E. (2008b) The iron isotope fingerprints of redox and biogeochemical cycling in modern and ancient earth. *Annu. Rev. Earth Planet. Sci.* **36**, 457–493.
Johnson C. M., Beard B. L. and Weyer S. (2020) Iron Geochemistry: An Isotopic Perspective. Springer.
Johnson C. M., Zheng X.-Y., Djokic T., Van Kranendonk M. J., Czaja A. D., Roden E. E. and Beard B. L. (2022) Early Archean biogeochemical iron cycling and nutrient availability: new insights from a 3.5 Ga land-sea transition. *Earth-Sci. Rev.* **228**, 103992.
Johnson J. E., Muhling J. R., Cosmidis J., Rasmussen B. and Templeton A. S. (2018) Low-Fe(III) greenalite was a primary mineral from Neoarchean Oceans. *Geophys. Res. Lett.* **45**, 3182–3192.
Kappler A. and Newman D. K. (2004) Formation of Fe(III)-minerals by Fe(II)-oxidizing photoautotrophic bacteria 1. *Geochim. Cosmochim. Acta* **68**, 1217–1226.
Kappler A., Newman D. K., Konhauser K. O. and Pasquero C. (2005) Deposition of banded iron formations by anoxygenic phototrophic Fe(II)-oxidizing bacteria. *Geology* **33**, 865–868.
Kappler A., Johnson C. M., Crosby H. A., Beard B. L. and Newman D. K. (2010) Evidence for equilibrium iron isotope fractionation by nitrate-reducing iron(II)-oxidizing bacteria. *Geochim. Cosmochim. Acta* **74**, 2826–2842.
Klein C. and Beukes N. J. (1992) Time distribution, stratigraphy, and sedimentologic setting, and geochemistry of Precambrian iron-formation. In *The Proterozoic Biosphere* (eds. J. W. Schopf and C. Klein). Cambridge University Press, Cambridge, pp. 139–146.
Koehler M. C., Buick R., Kipp M. A., Stüeken E. E. and Zaloumis J. (2018) Transient surface ocean oxygenation recorded in the ~2.66-Ga Jeerinah Formation, Australia. *Proc. Natl. Acad. Sci. U. S. A.* **115**, 7711–7716.
Konhauser K. O., Hamade T., Raiswell R., Morris R. C., Ferris F. G., Southam G. and Canfield D. E. (2002) Could bacteria have formed the Precambrian banded iron formations? *Geology* **30**, 1079.
Konhauser K. O., Planavsky N. J., Hardisty D. S., Robbins L. J., Warchola T. J., Haugaard R., Lalonde S. V., Partin C. A., Oonk P. B. H., Tsikos H., Lyons T. W., Bekker A. and Johnson C. M. (2017) Iron formations: a global record of Neoarchaean to Palaeoproterozoic environmental history. *Earth-Sci. Rev.* **172**, 140–177.
Li W., Czaja A. D., Van Kranendonk M. J., Beard B. L., Roden E. E. and Johnson C. M. (2013) An anoxic, Fe (II)-rich, U-poor ocean 3.46 billion years ago. *Geochim. Cosmochim. Acta* **120**, 65–79.
Li W., Beard B. L. and Johnson C. M. (2015) Biologically recycled continental iron is a major component in banded iron formations. *Proc. Natl. Acad. Sci. U. S. A.* **112**, 8193–8198.
Li Y.-L. (2014) Micro- and nanobands in late Archean and Palaeoproterozoic banded-iron formations as possible mineral records of annual and diurnal depositions. *Earth Planet. Sci. Lett.* **391**, 160–170.
Liu H., Wei Y. and Sun Y. (2005) The Formation of hematite from ferrihydrite using Fe(II) as a catalyst. *J. Mol. Catal. A-Chem.* **226**, 135–140.
Matsuo M., Kobayashi T. and Tsurumi M. (1994) Mössbauer spectroscopic characterization of iron compounds in paddy soil. *Hyperfine Interact.* **84**, 533–537.
Miot J., Benzerara K., Morin G., Kappler A., Bernard S., Obst M., Férard C., Skouri-Panet F., Guigner J.-M., Posth N., Galvez M., Brown G. E. and Guyot F. (2009a) Iron biomineralization by anaerobic neutrophilic iron-oxidizing bacteria. *Geochim. Cosmochim. Acta* **73**, 696–711.
Miot J., Benzerara K., Obst M., Kappler A., Hegler F., Schädler S., Bouchez C., Guyot F. and Morin G. (2009b) Extracellular iron biomineralization by photoautotrophic iron-oxidizing bacteria. *Appl. Environ. Microbiol.* **75**, 5586–5591.
Morris R. C. (1993) Genetic modelling for banded iron-formation of the Hamersley Group, Pilbara Craton, Western Australia. *Precambrian Res.* **60**, 243–286.
Polyakov V. B. and Mineev S. D. (2000) The use of Mössbauer spectroscopy in stable isotope geochemistry. *Geochim. Cosmochim. Acta* **64**(5), 849–865.
Porsch K. and Kappler A. (2011) FeII oxidation by molecular O2 during HCl extraction. *Environ. Chem.* **8**, 190–197.
Posth N. R., Konhauser K. O. and Kappler A. (2013) Microbiological processes in banded iron formation deposition. *Sedimentology* **60**, 1733–1754.
Raiswell R., Hardisty D. S., Lyons T. W., Canfield D. E., Owens J. D., Planavsky N. J., Poulton S. W. and Reinhard C. T. (2018) The iron paleoredox proxies: a guide to the pitfalls, problems and proper practice. *Am. J. Sci.* **318**, 491–526.
Rasmussen B., Krapež B. and Meier D. B. (2014) Replacement origin for hematite in 2.5 Ga banded iron formation: evidence for postdepositional oxidation of iron-bearing minerals. *Geol. Soc. Am. Bull.* **126**, 438–446.
Rasmussen B. and Muhling J. R. (2018) Making magnetite late again: evidence for widespread magnetite growth by thermal decomposition of siderite in Hamersley banded iron formations. *Precambr. Res.* **306**, 64–93.
Raye U., Pufahl P. K., Kyser T. K., Ricard E. and Hiatt E. E. (2015) The role of sedimentology, oceanography, and alteration on the δ56Fe value of the Sokoman Iron Formation, Labrador Trough, Canada. *Geochim. Cosmochim. Acta* **164**, 205–220.
Rouxel O. J., Bekker A. and Edwards K. J. (2005) Iron isotope constraints on the Archean and Paleoproterozoic Ocean Redox State. *Science* **307**, 1088–1091.
Rustad J. R., Casey W. H., Yin Q.-Z., Bylaska E. J., Felmy A. R., Bogatko S. A., Jackson V. E. and Dixon D. A. (2010) Isotopic fractionation of Mg2+(aq), Ca2+(aq), and Fe2 +(aq) with carbonate minerals. *Geochim. Cosmochim. Acta* **74**, 6301–6323.
Schad M., Halama M., Bishop B., Konhauser K. O. and Kappler A. (2019) Temperature fluctuations in the Archean ocean as trigger for varve-like deposition of iron and silica minerals in banded iron formations. *Geochim. Cosmochim. Acta* **265**, 386–412.

Schauble E. A. (2004) Applying stable isotope fractionation theory to new systems. *Rev. Mineral. Geochem.* **55**(1), 65–111.

Schwertmann U and Cornell R. M. (2000). *Iron oxides in the laboratory*. Wiley Online Library.

Skulan J. L., Beard B. L. and Johnson C. M. (2002) Kinetic and equilibrium Fe isotope fractionation between aqueous Fe(III) and hematite. *Geochim. Cosmochim. Acta* **66**, 2995–3015.

Slotznick S. P., Johnson J. E., Rasmussen B., Raub T. D., Webb S. M., Zi J.-W., Kirschvink J. L. and Fischer W. W. (2022) Reexamination of 2.5-Ga "whiff" of oxygen interval points to anoxic ocean before GOE. *Sci. Adv.* **8**, eabj7190.

Spinks S.C., Thorne R.L., Sperling, E., White, A., Armstrong, J., leGras, M., Birchall, R., Munday, T., 2018. Sedimentary Manganese as Precursors to the Supergene Manganese Deposits of the Collier Group; Capricorn Orogen, Western Australia. CSIRO, Australia. EP18235, pp. 36.

Stookey L. L. (1970) Ferrozine–-a new spectrophotometric reagent for iron. *Anal. Chem.* **42**, 779–781.

Swanner E. D., Wu W., Schoenberg R., Byrne J., Michel F. M., Pan Y. and Kappler A. (2015) Fractionation of Fe isotopes during Fe(II) oxidation by a marine photoferrotroph is controlled by the formation of organic Fe-complexes and colloidal Fe fractions. *Geochim. Cosmochim. Acta* **165**, 44–61.

Swanner E. D., Bayer T., Wu W., Hao L., Obst M., Sundman A., Byrne J. M., Michel F. M., Kleinhanns I. C., Kappler A. and Schoenberg R. (2017) Iron isotope fractionation during Fe(II) oxidation mediated by the oxygen-producing marine cyanobacterium synechococcus PCC 7002. *Environ. Sci. Technol.* **51**, 4897–4906.

Welch S. A., Beard B. L., Johnson C. M. and Braterman P. S. (2003) Kinetic and equilibrium Fe isotope fractionation between aqueous Fe(II) and Fe(III). *Geochim. Cosmochim. Acta* **67**, 4231–4250.

Wu L., Beard B. L., Roden E. E., Kennedy C. B. and Johnson C. M. (2010) Stable Fe isotope fractionations produced by aqueous Fe(II)-hematite surface interactions. *Geochim. Cosmochim. Acta* **74**, 4249–4265.

Wu L., Beard B. L., Roden E. E. and Johnson C. M. (2011) Stable iron isotope fractionation between aqueous Fe(II) and hydrous ferric oxide. *Environ. Sci. Technol.* **45**, 1847–1852.

Wu L., Percak-Dennett E. M., Beard B. L., Roden E. E. and Johnson C. M. (2012) Stable iron isotope fractionation between aqueous Fe(II) and model Archean ocean Fe–Si coprecipitates and implications for iron isotope variations in the ancient rock record. *Geochim. Cosmochim. Acta* **84**, 14–28.

Wu W., Swanner E. D., Hao L., Zeitvogel F., Obst M., Pan Y. and Kappler A. (2014) Characterization of the physiology and cell–mineral interactions of the marine anoxygenic phototrophic Fe (II) oxidizer Rhodovulum iodosum – implications for Precambrian Fe(II) oxidation. *FEMS Microbiol. Ecol.* **88**, 503–515.

Wu W., Swanner E. D., Kleinhanns I. C., Schoenberg R., Pan Y. and Kappler A. (2017) Fe isotope fractionation during Fe(II) oxidation by the marine photoferrotroph Rhodovulum iodosum in the presence of Si – implications for Precambrian iron formation deposition. *Geochim. Cosmochim. Acta* **211**, 307–321.

Xiong J. (2007) Photosynthesis: what color was its origin? *Genome Biol.* **7**, 245.

Yamaguchi K. E., Johnson C. M., Beard B. L. and Ohmoto H. (2005) Biogeochemical cycling of iron in the Archean-Paleoproterozoic Earth: constraints from iron isotope variations in sedimentary rocks from the Kaapvaal and Pilbara Cratons. *Chem. Geol.* **218**, 135–169.

Zhu C., Lu W., He Y., Ke S., Wu H. and Zhang L. (2018) Iron isotopic analyses of geological reference materials on MC-ICP-MS with instrumental mass bias corrected by three independent methods. *ACTA Geochim.* **37**, 691–700.

Associate editor: Dominik Weiss